Materials & Design 226 (2023) 111623

Contents lists available at ScienceDirect

Materials & Design

journal homepage: www.elsevier.com/locate/matdes

Large torsional rotation and rotational inversion coupling with linear deformation of electromechanical actuators based on conductive micro-/nano-helices

Lu Dai [a,*], Jia You [a], Wenzhong Shen [b,*], Ka-Di Zhu [b], Xiaojiang Huang [c]

[a] Jiangsu Key Laboratory of Micro and Nano Heat Fluid Flow Technology and Energy Application, School of Physical Science and Technology, Suzhou University of Science and Technology, Suzhou 215009, China

[b] Key Laboratory of Artificial Structures and Quantum Control (Ministry of Education), School of Physics and Astronomy, Shanghai Jiao Tong University, Shanghai 200240, China

[c] College of Science, Donghua University, Shanghai 201620, China

HIGHLIGHTS

- A comprehensive theory for quantitatively analyzing the electromechanical properties of conductive micro-/nano-helices is presented.
- The expressions of Hooke's constants are derived for conductive helices to conquer the difficulty of quantitative application.
- The currents or the voltages make the conductive micro-/nano-helices stronger.
- The close packed conductive micro-/nano-helices are for realizing the electromechanical actuators of coupled rotational inversion and large linear deformation.
- The non-close packed conductive micro-/nano-helices are for realizing the electromechanical actuators of larger torsional stroke of unwinding during the contraction.

GRAPHICAL ABSTRACT

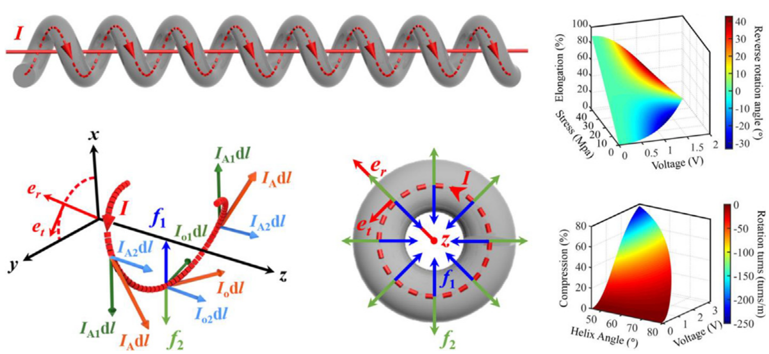

ARTICLE INFO

Article history:
Received 1 November 2022
Revised 21 December 2022
Accepted 11 January 2023
Available online 12 January 2023

Keywords:
Conductive micro-/nano-helices
Electromechanical actuators
Cosserat curve theory
Electromagnetic distributed forces
Electromechanical properties

ABSTRACT

A great variety of electrically conductive micro-/nano-helices provide the unique interconversion of torsional rotation and linear deformation, which makes them the excellent elements as electromechanical actuators in artificial muscle. In this paper, a comprehensive theory has been constructed for quantitatively analyzing the electromechanical properties involving coupled torsional rotation and linear deformation of the close packed and non-close packed electrically conductive helices with the aid of the concept of Cosserat curve. The distributed force in our model can be used to describe the resultant electromagnetic force and the internal pressure on the current carrying helices, which agree well with the experimental results. It is revealed that if the designers intend to realize the mechanical actuation of coupled rotational inversion and large axial contraction, they can choose the close packed conductive micro-/nano-helices; while if they want the much larger torsional stroke of unwinding during the contraction process, the non-close packed ones will be a good choice. The currents make both kinds of helices

* Corresponding authors.
E-mail addresses: dailu.1106@aliyun.com (L. Dai), wzshen@sjtu.edu.cn (W. Shen).

https://doi.org/10.1016/j.matdes.2023.111623
0264-1275/

stronger, and decreasing helix angle is an additional option for the non-close packed ones. The present study supplies a reliable theoretical reference for further experimental research on the applications of conductive helices in micro-/nanoelectromechanical systems.

1. Introduction

The science of the ubiquitous and fantastic helical structures in nature is one of the towering achievements of human intellect in its quest to understand our world and ourselves. Thanks to the rapid development of technology, the helical structures at the nanoscale dimension have been not only found and observed in organic beings, [1,2] but also realized in functional materials - among them the electrically conducting materials. There are a wide variety of conductive helices prepared by multiple approaches. Inserting twist in the carbon nanotube (CNT) fibers brings first the yarns then the microcoils with combined remarkable properties of high conductivity, high tensile strength and light weight [3,4]. Besides, the rolled up helical nanobelts composed of metal, metallic oxide and semiconductor heterostructures [5,6] can be obtained from the method that combines bottom-up thin film growth with top-down lithographic patterning [7–9]. To make full use of the gifts from nature, the micro helical structures of the xylem vessels, the plant fibers, the vascular bundles, the tracheary microfilaments are decorated with the conductive coating of metal, [10] metallic conjugated polymer [11] and polyaniline [12] through the biotemplating processes [13]. This idea of coating insulating materials with conductive layers is also applicable to the synthetic micro-/nano-helices [14–18].

These conductive micro-/nano-helices are excellent elements for electromechanical actuators as they provide unique interconversion of torsional rotation and linear deformation. In this respect, the CNT yarns and microcoils are most popular and intensively researched [19–22]. The CNT yarns are composed of tens to hundreds of helical fibers with a light weight of a linear density of 100 μgm^{-1} [23]. During the actuation processes, they exhibit excellent load stress over 100 times that of the strongest natural skeletal muscle, as well as high rotation stability without noticeable oscillation [24]. Even after 2400 cycles of reversible torsional actuation, the CNT yarns still completely recover the original state without load current [25–27]. Conversely, these CNT yarns can also be mechanically driven to generate electricity [28,29]. Twisting a CNT yarn produces a microcoil. The CNT microcoils retain not only the mechanical actuation of coupled torsional rotation and axial contraction under small voltages, but also the advantages of the CNT yarns of light weight, high torsional rotation stroke, good stability, fatigue resistance and reversibility. In addition, the tensile strokes have been improved to 14 % of contraction strain [30] and 90 % of tensile contraction strain, [31] and the strength capacity can be enhanced due to the helical structure [4]. These fascinating properties allow the CNT microcoils to function as artificial muscles, micro robots, rotational motors, electrodes, actuators, sensors, energy harvesters for diverse applications in both micro- and macro-electromechanical systems [32–38].

There are two kinds of guest-filled and guest-free CNT yarns. For the former ones, the phase transition of guest materials is the primary reason for radial expansion, axial contraction and torsional rotation of the CNT helices under the load voltage [20,24,39]. For the guest-free CNT yarns immersed in the electrolyte, such deformation is largely driven by ion insertion [19]. The above two mechanisms can be summarized to the internal pressure associated with yarn volume expansion. While for the guest-free CNT yarns in air, it is the Ampère force generated from current that leads to the linear and rotational deformation coupling [23,30,40–43]. Most importantly, this electromagnetic effect exists in all current carrying helical structures, and in some cases, the distributed forces from it are just relatively weak compared to that from other effects.

Therefore, it is necessary to explore the effect of current on the mechanical properties of conductive micro-/nano-helices from the perspective of the electromagnetic distributed forces. Besides, the conductive micro-/nano-helices in the experimental research are almost close packed helices, which brings the limitation for large-stroke contraction actuation under the condition without tensile force. In this paper, we provide a theoretical basis for the electromechanical properties involving linear and rotational deformation coupling of the close packed and non-close packed electrically conductive helical structures by employing the Cosserat rod model with four kinds of deformation of bending, torsion, extension and shear. A detailed analysis on the electromagnetic distributed forces agrees well with the experiments, then a set of expressions containing them are given to quantitatively measure the physical quantities including the Hooke's constants. It is found that the voltages strengthen the Hooke's constants as well as the load capacity of conductive micro-/nano-helices. The close packed conductive helices, in the elongated states under load forces, acquire the mechanical actuation of coupled rotational inversion and large axial contraction under extra load voltages until restore their original packed shape. While the current carrying non-close packed conductive helices exhibit the much larger torsional stroke of unwinding during the contraction process. Either decreasing helix angles or compressing helices can make them stronger, and the voltages give better results than the forces do. The present study suggests the appropriate kind of conductive micro-/nano-helices to design the large torsional and axial electromechanical actuators of both rotation and rotational inversion, depending on the applications requirements in artificial muscle.

2. Distributed magnetic forces

As shown in Fig. 1(a), an electrically conducting right-handed helix carries a steady current I. The direction of the current flow is represented by the red arrows.

As Fig. 1(b) shows, in order to find the distributed forces on the rod, the magnetic force on a current element of $I_o d\boldsymbol{l}$ is analyzed in detail based on cylindrical coordinates. The red three-dimensional dotted line indicates the current flowing through one turn of the helix. The helix axis is z-axis. The other two current elements of $I_A d\boldsymbol{l}$ are chosen at the points symmetric about the location of $I_o d\boldsymbol{l}$. And the azimuth θ between $I_o d\boldsymbol{l}$ and each $I_A d\boldsymbol{l}$ is smaller than 180°. The red dotted circular arc indicates the projection of the 3D helical line in the xoy plane, where the unit vector $\boldsymbol{e_r}$ points along the radial direction of helix and the unit vector $\boldsymbol{e_\theta}$ points along the direction of increasing azimuth θ. $\boldsymbol{e_\theta}$ is perpendicular to $\boldsymbol{e_r}$. $I_A d\boldsymbol{l_1}$ and $I_A d\boldsymbol{l_2}$ are the $\boldsymbol{e_\theta}$ and z components of $I_A d\boldsymbol{l}$, respectively. According to Biot–Savart law, the magnetic field at field point of $I_o d\boldsymbol{l}$ caused by a pair of current elements $I_A d\boldsymbol{l_1}$ can be decomposed into two components along -$\boldsymbol{e_\theta}$ and +z-direction. Then, according to Ampere's law, the magnetic force $\boldsymbol{f_1}$ on the current element $I_o d\boldsymbol{l}$ points along +$\boldsymbol{e_r}$-direction. Similarly, in the magnetic field along +$\boldsymbol{e_\theta}$-direction caused by the other pair of current elements $I_A d\boldsymbol{l_2}$, the magnetic force $\boldsymbol{f_2}$ on the current element $I_o d\boldsymbol{l}$ points along -$\boldsymbol{e_r}$-direction.

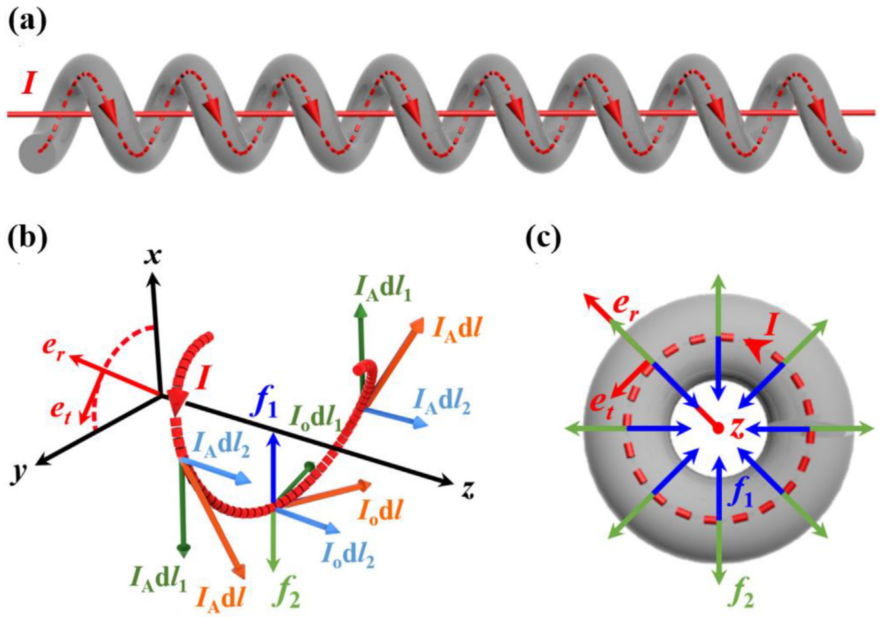

Fig. 1. (a) An electrically conducting right-handed helix carries a steady current I. (b) Analysis of the distributed magnetic force on a current element of $I_o dl$. (c) The cross section of helix.

Fig. 1(c) shows the cross section of helix. By symmetry, there are two kinds of distributed magnetic forces on a conductive helix of infinite length: $\boldsymbol{f_1}$ along +$\mathbf{e_r}$-direction and $\boldsymbol{f_2}$ along -$\mathbf{e_r}$-direction. An analysis of an electrically conducting left-handed helix reaches the same conclusion of distributed magnetic forces on the rods. Therefore, the distributed magnetic forces are parallel to the radial direction and lead to the radical and axial deformation of helix, which agree with the experiments [23,29,41,42]. It is reported that the yarn volume expansion, the result of the ion insertion and the phase transition of the materials, is the other reason for such deformation of helix [19,20,24,39].

3. Close packed conductive micro-/nano-helices

3.1. Modeling

As shown in Fig. 2(a), to establish the Cosserat curve model for exploring the electromechanical behavior of conductive micro-/nano-helices, we assume that a close packed helix H_{0A} with the radius a_{0A}, the pitch b_{0A}, and the number of coils N_1, is loaded under a force F along its helix axis to transform to the elongated helix H_{0F} of radius a_{0F} and pitch b_{0F}. When a constant bias voltage is applied, the elongated helix H_{0F} shrinks along its helix axis and transforms to the current I carrying helix H_1 with the radius a_1, the pitch b_1. During the whole loading process, the ends of helix are prevented from rotating. The number of coils of H_{0F} and H_1 remain N_1. As Fig. 2(b) shows, if the loading end of helix H_{0A} is allowed to rotate under the applied force and current, it changes to the helix H_2 with the radius a_2, the pitch b_2, the number of coils N_2. The cross section of coil wire is circle and its radius r is assumed to be constant. $\boldsymbol{D}_i$ (i = 1, 2, 3) are the director basis of H_{0A} and $\boldsymbol{d}_i$ are the director basis of the deformed helices, which are defined by a set of Euler angles φ_0, θ_0, ψ_0 and φ, θ, ψ, respectively [44]. We choose the first director $\boldsymbol{D}_1/\boldsymbol{d}_1$ and the second director $\boldsymbol{D}_2/\boldsymbol{d}_2$ along the direction of the largest and smallest bending stiffness of the cross section of corresponding helical structure, and the helix axis along the $\boldsymbol{e_3}$ axis of the fixed Cartesian basis. For such a case the director deformation measures $W(0)$ of H_{0A} and W of the deformed helices have the form of:

$$\begin{aligned} &W_1^{(0)} = 0,\ W_2^{(0)} = \dot{\psi}_0 \sin\theta_0,\ W_3^{(0)} = \dot{\psi}_0 \cos\theta_0 \\ &W_1 = 0,\ W_2 = \hat{\psi} \sin\theta,\ W_3 = \hat{\psi} \cos\theta \end{aligned} \tag{1}$$

$\widehat{(\cdot)} = \partial(\cdot)/\partial\boldsymbol{S}$ and $\dot{(\cdot)} = \partial(\cdot)/\partial\boldsymbol{s}$ is the stretch of the curve with S the arc length along the fixed reference configuration of H_{0A} and s the one along the deformed configurations of H_{0F}, H_1 and H_2. For the configuration of helix θ_0, $\dot{\boldsymbol{\psi}}_0$, θ, $\widehat{\boldsymbol{\psi}}$ are all constants [45].

Based on the Cosserat curve model of a helical structure with distributed forces, [46] we have the radius and pitch of helix H_{0A}:

$$a_{0A} = \sin\theta_0/\dot{\psi}_0,\ b_{0A} = 2\pi\cos\theta_0/\dot{\psi}_0 \tag{2}$$

where

$$\dot{\psi}_0 = 2\pi N_1/L_0 \tag{3}$$

and $L_0 = N_1\sqrt{(2\pi a_{0A})^2 + b_{0A}^2}$ is the length of the coil wire of H_{0A}. The radius and pitch of helix $H_1(H_2)$ are given by:

$$\begin{aligned} a_1(a_2) &= \frac{1}{\hat{\psi}}\left[\left(-\frac{F}{E_2}\sin\theta - \frac{f}{\hat{\psi}}\frac{1}{E_2}\cos\theta\right)\cos\theta \right.\\ &\qquad \left. + \left(\frac{F}{E_3}\cos\theta - \frac{f}{\hat{\psi}}\frac{1}{E_3}\sin\theta + 1\right)\sin\theta\right] \\ b_1(b_2) &= \frac{2\pi}{\hat{\psi}}\left[\left(\frac{F}{E_2}\sin\theta + \frac{f}{\hat{\psi}}\frac{1}{E_2}\cos\theta\right)\sin\theta \right.\\ &\qquad \left. + \left(\frac{F}{E_3}\cos\theta - \frac{f}{\hat{\psi}}\frac{1}{E_3}\sin\theta + 1\right)\cos\theta\right] \end{aligned} \tag{4}$$

where

$$\hat{\psi} = 2\pi N_2/L_0 \tag{5}$$

and $E_2 = K_2 G\pi r^2$ and $E_3 = E\pi r^2$. E and $G = E/[2(1 + v)]$ are the Young's and shear moduli, respectively. v is the Poisson's ratio. K_2 is the Timoshenko shear coefficients and related to v through $K_2 = \left[6(1+v)^2\right]/\left[7 + 12v + 4v^2\right]$[47]. For the helix H_1 with two ends restricted from rotating, we have

$$\hat{\psi} = \dot{\psi}_0 \tag{6}$$

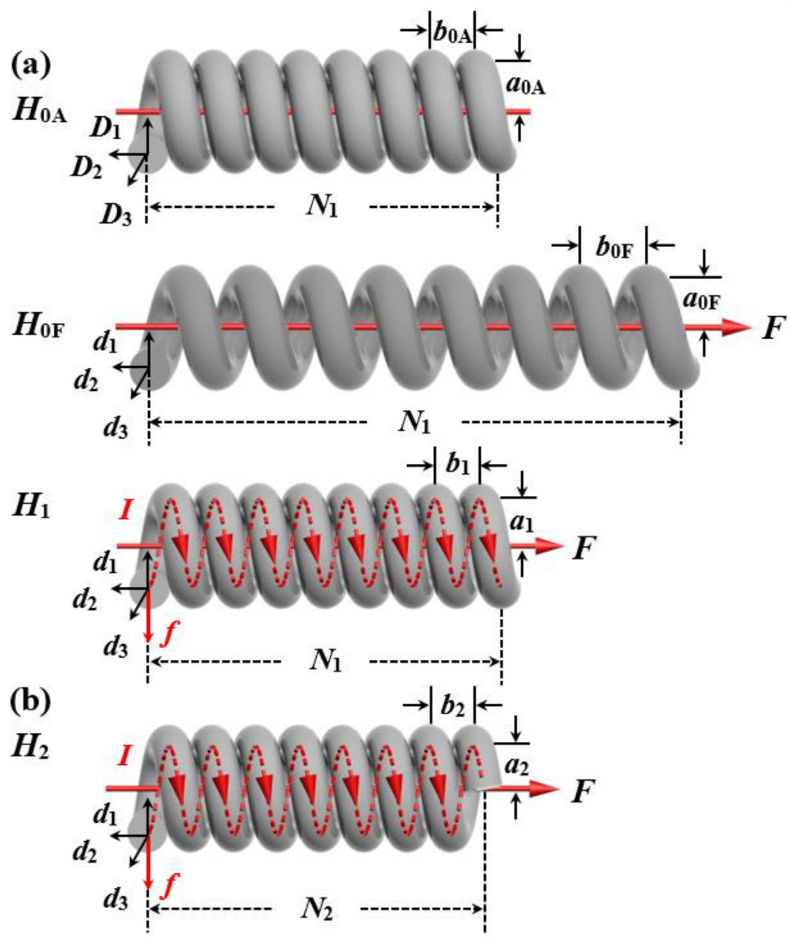

Fig. 2. Configurations of (a) the unloaded state H_{0A}, the tensile force F loaded state H_{0F}, and the extra current I loaded state H_1 of a close packed helix whose ends are prevented from rotating, (b) as well as the loaded state H_2 of a close packed helix whose end is allowed to rotate under the applied force F and current I.

For the helix H_2 with one end free to rotate, we have

$$\hat{\psi} = \frac{B\sin\theta_0\sin\theta + C\cos\theta_0\cos\theta}{B\sin^2\theta + C\cos^2\theta}\dot{\psi}_0 \tag{7}$$

where $B = EJ_1$, $C = GJ_2$. $J_1=(\pi r^4)/4$ is the moment of inertia and $J_2=(\pi r^4)/2$ is the polar moment of inertia of the cross section. The equilibrium equation of deformed helices is given by:

$$\begin{aligned}&\left(\tfrac{1}{E_3}-\tfrac{1}{E_2}\right)\sin\theta\cos\theta F^2+\left[\sin\theta+\left(\tfrac{1}{E_3}-\tfrac{1}{E_2}\right)\left(\cos^2\theta-\sin^2\theta\right)\tfrac{f}{\hat{\psi}}\right]F\\&+B\hat{\psi}\left(\hat{\psi}\sin\theta-\dot{\psi}_0\sin\theta_0\right)\cos\theta-C\hat{\psi}\sin\theta\left(\hat{\psi}\cos\theta-\dot{\psi}_0\cos\theta_0\right)\\&-\left(\tfrac{1}{E_3}-\tfrac{1}{E_2}\right)\sin\theta\cos\theta\left(\tfrac{f}{\hat{\psi}}\right)^2+\cos\theta\tfrac{f}{\hat{\psi}}=0\end{aligned} \tag{8}$$

where the distributed force $\boldsymbol{f}=f\,\boldsymbol{d_1}$ and is parallel to the radial direction [46]. The electromagnetic force, as well as the internal pressure associated with yarn volume expansion, both lead to the radical and axial deformation of helix. The distributed force $\boldsymbol{f}$ is able to describe the resultant force on rod. The Hooke's constant h_1 of H_1 is given by Hooke's law: $h_1 = \mathrm{d}F/\mathrm{d}(N_1b_1)$. From equations (4) and (8), we have the form of

$$\begin{aligned}&h_1=-Q_1Q_3/(Q_1Q_4+Q_2),\\&Q_1\equiv\left(\tfrac{1}{E_3}-\tfrac{1}{E_2}\right)\left(\sin\theta-\tfrac{\cos^2\theta}{\sin\theta}\right)F^2-\tfrac{\cos\theta}{\sin\theta}F\\&\qquad+B\dot{\psi}_0{}^2\left[(\sin\theta-\sin\theta_0)-\tfrac{\cos^2\theta}{\sin\theta}\right]-C\dot{\psi}_0{}^2\left[\sin\theta-(\cos\theta-\cos\theta_0)\tfrac{\cos\theta}{\sin\theta}\right]\\&\qquad+\left[4\cos\theta\left(\tfrac{1}{E_3}-\tfrac{1}{E_2}\right)\tfrac{F}{\dot{\psi}_0}-\left(\tfrac{1}{E_3}-\tfrac{1}{E_2}\right)\left(\sin\theta-\tfrac{\cos^2\theta}{\sin\theta}\right)\tfrac{f}{\dot{\psi}_0{}^2}+\tfrac{1}{\dot{\psi}_0}\right]f,\\&Q_2\equiv2F\left(\tfrac{1}{E_3}-\tfrac{1}{E_2}\right)\sin\theta\cos\theta+\sin\theta+\left(\tfrac{1}{E_3}-\tfrac{1}{E_2}\right)\left(2\cos^2\theta-1\right)\tfrac{f}{\dot{\psi}_0},\\&Q_3\equiv L_0^{-1}\left[2F\left(\tfrac{1}{E_3}-\tfrac{1}{E_2}\right)\cos\theta+1-\tfrac{f}{\dot{\psi}_0}\left(\tfrac{1}{E_3}-\tfrac{1}{E_2}\right)\left(\sin\theta-\tfrac{\cos^2\theta}{\sin\theta}\right)\right]^{-1},\\&Q_4\equiv-\left(\tfrac{\sin^2\theta}{E_2}+\tfrac{\cos^2\theta}{E_3}\right)\times\\&\left[2F\left(\tfrac{1}{E_3}-\tfrac{1}{E_2}\right)\cos\theta+1-\tfrac{f}{\dot{\psi}_0}\left(\tfrac{1}{E_3}-\tfrac{1}{E_2}\right)\left(\sin\theta-\tfrac{\cos^2\theta}{\sin\theta}\right)\right]^{-1}.\end{aligned} \tag{9}$$

The Hooke's constant h_2 of H_2 is given by Hooke's law: $h_2 = \mathrm{d}F/\mathrm{d}(N_2b_2)$. From equations (4), (7) and (8), we have the form of

$$\begin{aligned}&h_2=-P_1P_3/(P_1P_4+P_2),\\&P_1\equiv\left(\tfrac{1}{E_3}-\tfrac{1}{E_2}\right)\left(\sin\theta-\tfrac{\cos^2\theta}{\sin\theta}\right)F^2-\tfrac{\cos\theta}{\sin\theta}F\\&+(B-C)\left[\hat{\psi}^2\left(\sin\theta-\tfrac{\cos^2\theta}{\sin\theta}\right)+2P_0\hat{\psi}\sin\theta\cos\theta\right]\\&+\left[-B\dot{\psi}_0\sin\theta_0\left(P_0\cos\theta+\hat{\psi}\right)+C\dot{\psi}_0\cos\theta_0\left(P_0\sin\theta-\tfrac{\cos\theta}{\sin\theta}\hat{\psi}\right)\right]\\&+\left(\tfrac{1}{E_3}-\tfrac{1}{E_2}\right)\left[-\left(\sin\theta-\tfrac{\cos^2\theta}{\sin\theta}\right)+2\sin\theta\cos\theta\tfrac{P_0}{\hat{\psi}}\right]\left(\tfrac{f}{\hat{\psi}}\right)^2\\&+\left[\begin{array}{l}4\cos\theta\left(\tfrac{1}{E_3}-\tfrac{1}{E_2}\right)\tfrac{F}{\hat{\psi}}+P_0\left(\tfrac{1}{E_3}-\tfrac{1}{E_2}\right)\left(1-2\cos^2\theta\right)\tfrac{F}{\hat{\psi}^2}\\+\tfrac{1}{\hat{\psi}}\left(1-\tfrac{\cos\theta}{\hat{\psi}}P_0\right)\end{array}\right]f,\end{aligned}$$

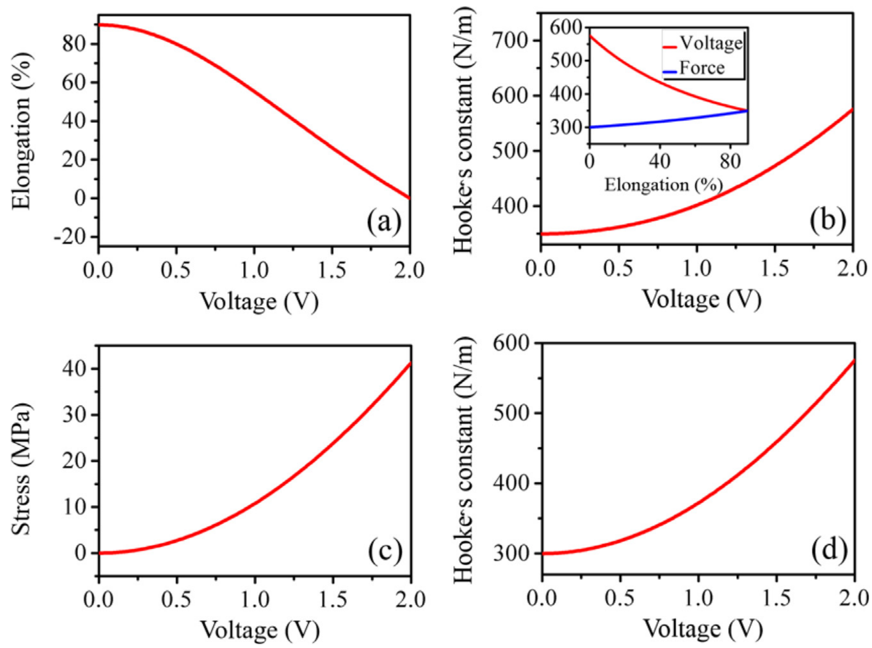

Fig. 3. (a) Elongation and (b) Hooke's constant versus voltage of a wax-SWNT helical yarn under a fixed axial force of 3.32 N. The inset shows Hooke's constant versus elongation under force load (the blue line) and under extra voltage load (the red line). (c) Stress and (d) Hooke's constant versus voltage of a close packed helix H_1 in its original length. (For interpretation of the references to colour in this figure legend, the reader is referred to the web version of this article.)

$$P_2 \equiv 2F\left(\tfrac{1}{E_3}-\tfrac{1}{E_2}\right)\sin\theta\cos\theta+\sin\theta+\left(\tfrac{1}{E_3}-\tfrac{1}{E_2}\right)\left(2\cos^2\theta-1\right)\tfrac{f}{\hat{\psi}},$$

$$P_3 \equiv L_0^{-1}\left\{\begin{array}{l} 2F\left(\tfrac{1}{E_3}-\tfrac{1}{E_2}\right)\cos\theta+1 \\ -f\left(\tfrac{1}{E_3}-\tfrac{1}{E_2}\right)\left[\tfrac{1}{\hat{\psi}}\left(\sin\theta-\tfrac{\cos^2\theta}{\sin\theta}\right)-\tfrac{P_0}{\hat{\psi}^2}\sin\theta\cos\theta\right]\end{array}\right\}^{-1},$$

$$P_4 \equiv -\left(\tfrac{\sin^2\theta}{E_2}+\tfrac{\cos^2\theta}{E_3}\right)\times$$

$$p\left\{\begin{array}{l} 2F\left(\tfrac{1}{E_3}-\tfrac{1}{E_2}\right)\cos\theta+1 \\ -f\left(\tfrac{1}{E_3}-\tfrac{1}{E_2}\right)\left[\tfrac{1}{\hat{\psi}}\left(\sin\theta-\tfrac{\cos^2\theta}{\sin\theta}\right)-\tfrac{P_0}{\hat{\psi}^2}\sin\theta\cos\theta\right]\end{array}\right\}^{-1},$$

$$P_0 \equiv \dot{\psi}_0\left(B\sin^2\theta+C\cos^2\theta\right)^{-2}\times$$

$$\left[\begin{array}{l}\left(B\sin^2\theta+C\cos^2\theta\right)\left(-B\sin\theta_0\tfrac{\cos\theta}{\sin\theta}+C\cos\theta_0\right) \\ +2\cos\theta(B-C)(B\sin\theta_0\sin\theta+C\cos\theta_0\cos\theta)\end{array}\right]. \tag{10}$$

Since $\boldsymbol{d_1}$ lies in the opposite direction of $\boldsymbol{e_r}$, the distributed magnetic forces $\boldsymbol{f_1}$ and $\boldsymbol{f_2}$ on a conductive helix illustrated in Fig. 1 are along -$\boldsymbol{d_1}$-direction and along +$\boldsymbol{d_1}$-direction: $\boldsymbol{f_1} = -f_1\boldsymbol{d_1}$ and $\boldsymbol{f_2} = f_2\boldsymbol{d_1}$. Then in equation (8) $f = f_2$-$f_1$and the f represents the total distributed magnetic force introduced by the current I.

3.2. Results

In order to quantitatively analyze the electromechanical performance of conductive micro-/nano-helices, we use the electromechanical actuators based on wax-SWNT helical yarn [31] as an example within the framework of the proposed Cosserat curve model. The close packed helix H_{0A} has the radius a_{0A} = 160 μm, the pitch b_{0A} = 191 μm, and the number of coils N_1 = 60. The elongated helix H_{0F} has the pitch b_{0F} = 363 μm. In the experiments, when a constant bias voltage of 2 V was applied, the helical yarn shrunk to its original length with two ends restricted from winding. Therefore, the current carrying helix H_1 has the radius a_1 = 160 μm and the pitch b_1 = 191 μm. The coil wire radius is r = 93 μm.

With the aid of the tensile stress–strain curve of a helical yarn tested without voltage in the Fig. 4d of reference 31, the average Young's modulus of wax-SWNT of E = 12 GPa and the axial loads of elongated helix H_{0F} of F = 3.32 N are derived from equations (2)–(4) and (8) with the distributed force f = 0. In the calculation, the geometric parameters of H_{0A} and H_{0F}, as well as the Poisson's ratio v = 0.279 [48] are used.

We further get the distributed force on H_1 of f = -1.2 × 10^5N/m from the above three equations with the geometric parameters of H_{0A} and H_1, the material parameters of average Young's modulus and Poisson's ratio, as well as the axial loads F. As shown in Fig. 2(b), the negative value of f indicates that the distributed force on rod, marked by the red arrow, is perpendicular to the helix axis and in the opposite direction to $\boldsymbol{d}_1$. These distributed forces, which are not just parallel to but also along the radial direction, lead to the radial expansion and axial contraction deformation of helix, as illustrated in the experiments [31].

When the electric pulse trains were applied in a neat CNT helix and a paraffin-infiltrated CNT helix, respectively, the actuations estimated by the tension change for both cases increased to their maximum value at the same time after inputting electric power [49]. The tension change of the paraffin-infiltrated CNT helix is larger than that of the neat one. Furthermore, both kinds of CNT helices have the same kind of the radial expansion and axial contraction. It suggests that there must be the electromagnetic distributed forces on the current carrying helices, while the phase transition of guest materials just strengthens the electromechanical effects. Since the electromagnetic effect exists in all current carrying helical structures, and in some cases, the distributed forces from it are just relatively weak compared to that from other effects, e.g. heating effect. As a result, we will concentrate on the electromagnetic part of the distributed forces originated from the applied voltage. According to Biot–Savart law, Ampere's law and Ohm's

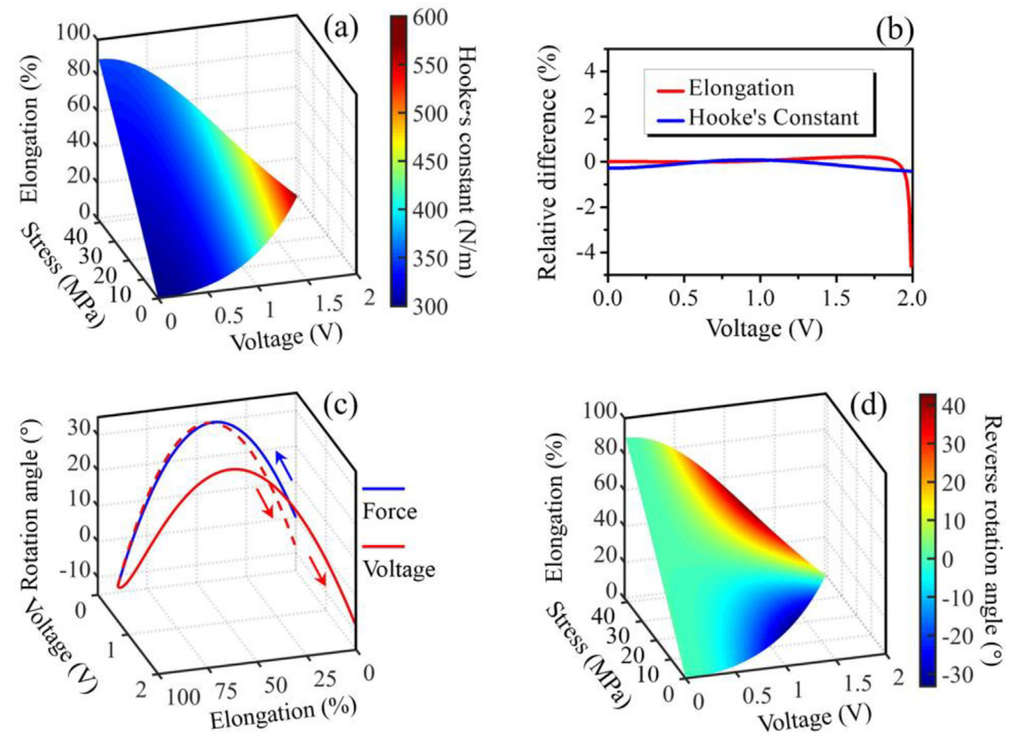

Fig. 4. (a) Elongation and Hooke's constant versus voltage as well as stress of a helix H_2. (b) Relative differences of the elongation (the red line) and the Hooke's constant (the blue line) between the two conditions that the load end cannot and can rotate freely. (c) Rotation angle versus elongation under force load (the blue line). Rotation angle versus elongation (the red dashed line), as well as versus voltage (the red line) under extra voltage load. (d) Elongation and reverse rotation angle versus voltage as well as stress of a helix H_2. (For interpretation of the references to colour in this figure legend, the reader is referred to the web version of this article.)

law, as well as the principle of virtual work or the law of the lever, [42] the distributed force is proportional to the square of the voltage U or the current I:

$$f = \alpha U^2 \tag{6a}$$

$$f = \beta I^2 \tag{6b}$$

where α and β are the scale coefficients. We have α = -3.0 $\times$ 10^4N/m·V^2 from the known constant bias voltage of 2 V and the distributed force. Equation (6a) and its fitting coefficient α ensure the reliability of the following quantitatively analysis of electromechanical properties for the close packed and non-close packed electrically conductive helices. If the applied currents are known, the distributed force can be derived from equation (6b).

A systematic study on the electromechanical properties of conductive micro-/nano-helices is performed based on the continuous increment of loads from 0 to the maximum value of F = 3.32 N and U = 2 V. Fig. 3a illustrates the elongation versus the voltage of the wax-SWNT helical yarn loaded under a fixed axial force of 3.32 N, using equations (2)–(4), (6), (8) and (11). The axial elongation of the helix decreases from 90 % to 0 % with increasing the voltage from 0 V to 2 V. In the latter part of the contraction, the curve is almost linear. Fig. 3b shows the dependence of the Hooke's constant on the voltage during this process of contraction from equation (9). The Hooke's constant increases from 349.4 N/m to 575.5 N/m, up 64.7 % due to the voltage. As shown in the inset, the previous load force stretches the helix and raises the Hooke's constant from 299.8 N/m to 349.4 N/m with the increment of 16.5 % (the blue line), while the load voltage further strengthens the load capacity to a greater extent (the red line). The load ability of a current carrying helix without deformation is useful in the artificial muscle. Fig. 3c and 3d presents how the stress and the Hooke's constant depends on the load voltage when the close packed helix maintains its original length, respectively, based on equations (2)–(4), (6), (8), (9) and (11). The higher voltage leads to the higher stress, defined by the load force per cross section area, and the larger Hooke's constant, which agrees well with the experimental restult of the larger axial contraction of helical yarns under larger load voltages [27]. Under the voltage of 2 V, the stress is 41.3 MPa and the Hooke's constant is 575.5 N/m, i.e. 1.9 times that of the unload state.

The loading end must be allowed to rotate under the applied force and voltage, if a current carrying helix serves as a torsional artificial muscle to provide unique mechanical actuation involving coupled torsional rotation and axial contraction. The wax-SWNT helical yarn is still regard as the close packed helix H_{0A}, which changes to the helix H_2 with a freely rotating end under loads (Fig. 2(c)). Fig. 4a shows the dependence of the elongation and the Hooke's constant on the voltage as well as the stress, from equations (2)–(4), (7), (8), (10) and (11). The close packed helix is loaded under an axial force F of 3.31 N to transform to the elongated one with the axial elongation of 90 %, then is loaded under a constant bias voltage of 2 V to shrink to its original length with the Hooke's constant of 592.9 N/m and the stress of 41.2 MPa.

Fig. 4b illustrates the relative differences of the elongation (the red line) and the Hooke's constant (the blue line) between the two conditions that the load end cannot and can rotate freely. The helices are under a fixed axial force of 3.31 N. The relative differences are the measure of the differences between the physical quantities of the helix H_2 and the helix H_1, in comparison to the corresponding ones of the helix H_1. The variation range of the relative differences of the elongation are 0.02 % $\sim$ 0.03 % and -0.01 % $\sim$ -4.60 %, for the voltage of 0 $\sim$ 1.88 V and 1.89 V $\sim$ 1.99 V, respectively. The variation range of the relative differences of the Hooke's constant increases from -0.28 % to 0.09 % and then decreases from

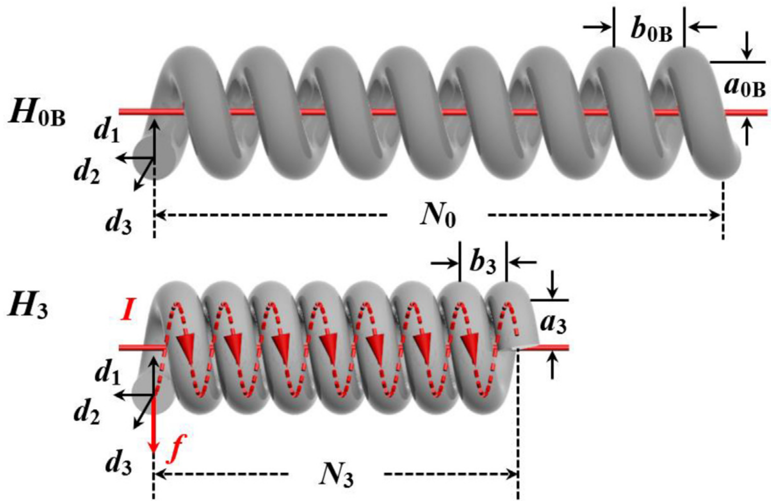

Fig. 5. Configurations of the unloaded state H_{0B} and the current I loaded state H_3 of a non-close packed helix whose end is allowed to rotate.

0.09 % to -0.42 %, for the voltage of 0 $\sim$ 0.94 V and 0.95 V $\sim$ 1.99 V, respectively. There are only minor differences in both the elongation and the Hooke's constant between the two conditions. The results show that the electrically conductive helices, whose loading ends are allowed to rotate under the applied force and voltage, can replace the ones that are prevented from rotating, when it comes to the application of the mechanical properties related to the axial deformation.

After describing the physical quantities of axial deformation for the helix H_2, the ones of coupled rotation and axial contraction are given. Fig. 4c illustrates the rotation angle, i.e. $(N_2 - N_1) \times 360°$, versus the axial elongation under loads, derived from equations (2)–(4), (5), (7), (8) and (11). At the stage of load force from 0 N to 3.31 N, the helix overwinds in the beginning of axial extension, and then unwinds when elongation is further increased (the blue line), which have been observed in some gourd and cucumber tendril perversions [50]. At the following stage of fixed load force of 3.31 N and load voltage from 0 V to 2 V, the helix rotates reversely and also exhibits the peculiar rotational inversion (the red line). To compare these two processes, we project the curve of the latter stage on the plane of the blue one (the red dashed line). Although the two curves on the Elongation-Rotation angle plane are not entirely coincidence, the difference is negligible. In comparison with the original shape, the helix unwinds -7.7°, which is only about 1.9×10^{-3} turn per millimeter. The helix can be regarded as be in its original close packed shape under both loads. To figure out the impact of the voltage on the rotary motion of helix, we define the reverse rotation angle as $(N_2 - N_{20}) \times 360°$, where N_{20} is the number of the force loaded helix. Fig. 4d shows the reverse rotation angle of the complete continuous loads. In the region of load force 0 N $\sim$ 1.47 N, the helix overwinds and extends 0 % $\sim$ 41.6 %, then contract and unwinds 0° $\sim$ 33° under the voltage 0 V $\sim$ 1.31 V. While in the region of load force 1.47 V $\sim$ 3.31 V, the helix shows the rotational inversion of overwinding followed by unwinding under both loads. Designers can choose the appropriate stretching region to realize the coupled fixed directional/bi-directional rotation and axial deformation.

4. Non-close packed conductive micro-/nano-helices

4.1. Modeling

In order to focus on the effect of the current on the electromechanical behavior of the coupled rotation and axial contraction of conductive micro-/nano-helices, we suppose that the loading end of a non-close packed helix is allowed to rotate under the only applied voltage. As Fig. 5 shows, a non-close packed helix H_{0B} with the radius a_{0B}, the pitch b_{0B}, the number of coils N_0 and the coil wire radius r, is loaded under a constant bias voltage to transform to the compressed helix H_3 of the radius a_3, the pitch b_3, and the number of coils N_3.

4.2. Results

The helix H_{0B} and the close packed helix H_{0A} have the same material parameters and geometry parameters, including the length and the radius of coil wire, as well as the number of coils. The radius a_{0B} and the pitch b_{0B} continuously change to obtain the helix H_{0B} with the helix angle, defined as $\zeta = \text{Arccos}\left[b_{0B}/\sqrt{(2\pi a_{0B})^2 + b_{0B}^2}\right] \times 180/\pi$, from 45° to 79.2° of H_{0A}.

We start with the physical quantities of axial deformation for the helix H_3. Fig. 6(a) presents and the Hooke's constant h_2 versus the axial compression and the load voltage in the range of helix angle $45° \le \zeta \le 79.2°$, deduced from equations (2)–(5), (7), (8), (10), (11) and the load force $F = 0$. When $\pi a_3 b_3/\sqrt{(2\pi a_3)^2 + b_3^2} - r = 0$, the loaded helix H_3 is compressed to its close packed state. In the range of $60° \le \zeta \le 79.2°$, the voltage enhances the Hooke's constant: for ζ = 60°, the helix is compressed to 65.45 % of its original length and its Hooke's constant increases from 394.52 N/m to 690.87 N/m under the voltage from 0 V to 2.58 V; while for ζ = 79.2°, the helix is compressed to 0.19 % of its original length and its Hooke's constant increases from 299.30 N/m to 301.58 N/m under the voltage from 0 V to 0.19 V. In the range of $45° \le \zeta \le 59.9°$, the Hooke's constant first decreases then increases with increasing the voltage: for ζ = 45°, the helix is compressed to 34.70 % of its original length and its Hooke's constant decreases from 597.24 N/m to 457.06 N/m under the voltage from 0 V to 1.52 V, then it is further compressed to 78.68 % and the Hooke's constant increases from 457.06 N/m to 878.36 N/m under the voltage from 1.52 V to 3.2 V. The result shows that the no load Hooke's constant is larger for smaller helix angle. The loaded close packed helix of ζ = 45° has the strongest load capacity because its Hooke's constant is three times that of ζ = 79.2°.

In Fig. 6(c), the Hooke's constants of the loaded close packed helices are compared between the situations of load force and load voltage, in the range of helix angle $45° \le \zeta \le 79.2°$. For the same

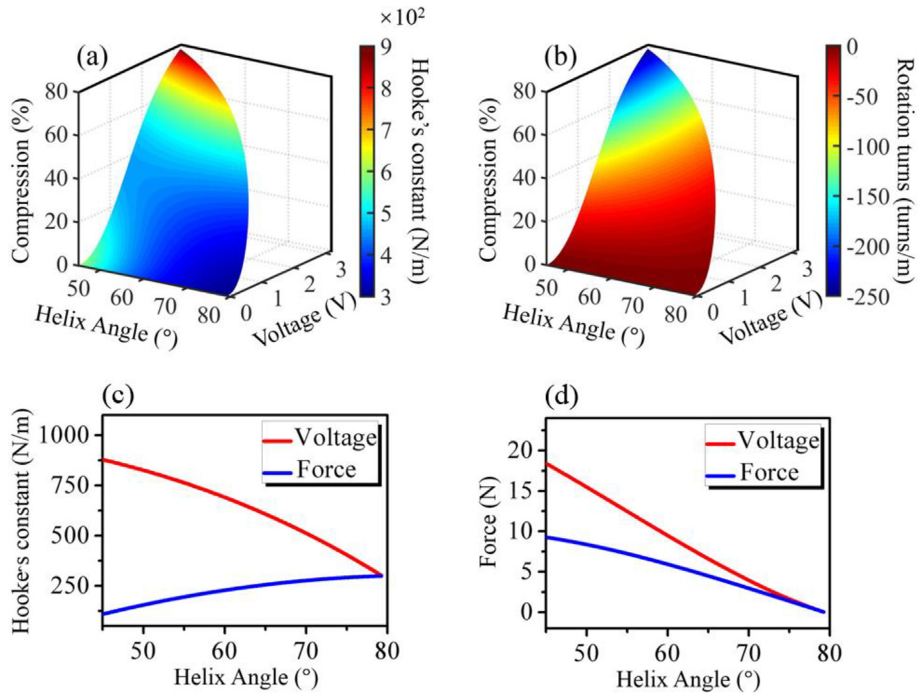

Fig. 6. (a) Hooke's constant, (b) rotation turns and compression versus voltage as well as stress of a helix H_3. (c) Hooke's constant and (d) Force versus helix angle of the loaded close packed states of helices under voltage load (the red line) and force load (the blue line). (For interpretation of the references to colour in this figure legend, the reader is referred to the web version of this article.)

helix angle, the Hooke's constant of the helix loaded by constant bias voltage (the red line) is larger than that of the one loaded by axial force (the blue line), from equations (2)–(5), (7), (8), (10), (11) and $f = 0$. The red line shows that the smaller helix angle leads to the larger Hooke's constant for the current carrying helices: the largest Hooke's constant of 878.36 N/m arises in $\zeta = 45°$, which is 8 times that of the force loaded helix.

Fig. 6(d) shows the further comparative study of the load ability for the loaded close packed states of helices between the situations of load force and load voltage. According to the Hooke's law, the load force is from the area under the curve of the Hooke's constant changing with the compression. For the same helix angle, the load force of the helix loaded by constant bias voltage (the red line) is larger than that of the one loaded by axial force (the blue line). The red line implies at the smaller helix angle leads to the larger load for the current carrying helices: the largest load force of 18.38 N arises in $\zeta = 45°$, which is 2 times that of the force loaded helix.

The physical quantities of coupled rotation and axial contraction are as follows. Fig. 6(b) displays the rotation turns of (N_3–N_0) and the torsional modulus versus the load voltage in the range of helix angle $45° \leq \zeta \leq 79.2°$, using equations (2)–(5), (7), (8), (11) and the load force $F = 0$. The helices just unwind in the entire compression process, which is consistent with the experimental results of the CNT microcoils without load force [19,23,30,31,34,51]. The rotation turns increase linearly with decreasing the helix angle: in the close packed states, the rotation turns are 0.3 turn per meter and 217.9 turns per meter for the helix angle of 79.2° and 45°, respectively.

To compare the rotation ability of the close packed helix H_2 and the helix H_3, it is noticed that in Fig. 4(c), during the whole compression process under the voltage, the initial state is the helix H_{0F} loaded by the maximum force of 3.31 N, i.e., the intersection point of lines, and final state is the helix H_2 loaded by the additional voltage of 1.99 V, i.e., the other end point of the red line. The compression is 47.4 % of the length of helix H_{0F} and the rotation angle is 41.89°, which is 5.33 turns per meter. Fig. 6(b) shows that the helix H_3 with $\zeta = 69.88°$ has the same compression of 47.4 % in the close packed states. While its rotation turns are 50.36 turns per meter, which is 9.4 times that of the helix H_2.

5. Conclusion

We have made a quantitative research on the electromechanical properties involving coupled torsional rotation and linear deformation of the close packed and non-close packed conductive micro-/nano-helices by applying the concept of Cosserat curve. According to Biot–Savart law and Ampere's law, the distributed magnetic forces on a conductive helix are parallel to the radial direction, which agree with the experimental results. It is found that the distributed force in the Cosserat curve model is able to describe the resultant electromagnetic force, as well as the internal pressure associated with yarn volume expansion. Since the Hooke's constants of conductive helices vary during the loading process, the expression is derived to conquer the difficulty of quantitative application. The higher voltages lead to the larger Hooke's constants and higher load capacity. When it comes to the application of the mechanical properties related to the axial deformation, the close packed conductive micro-/nano-helices with rotating load ends can replace the ones without. Moreover, this kind of helices exhibit the rotational inversion in the elongation process under load forces, as well as in the following contraction process under extra voltage load until recover the original packed shape. For the non-close packed conductive micro-/nano-helices, the ones with the fixed number of coils and the smaller helix angles are more though. In the entire coupled rotation and axial contraction process, the helices just unwind. The voltage makes the helices stronger than the force does. A further comparative study between a close packed helix and a non-close packed helix shows that the rotation turns of the latter are 9.4 times that of the former for the same compression of 47.4 %. The present study helps the designers choose the appropriate kind of conductive micro-/nano-helices to realize the large torsional and axial electromechanical actuation driven by electricity of both rotation and rotational inversion, depending on the applications requirements in artificial muscle.

Data availability

Data will be made available on request.

Declaration of Competing Interest

The authors declare that they have no known competing financial interests or personal relationships that could have appeared to influence the work reported in this paper.

Acknowledgement

This work was supported by the National Natural Science Foundation of China (Nos. 11904249, 11974242 and 11834011), and the Natural Science Foundation of Shanghai (No. 20ZR1429900).

References

[1] J.D. Watson, F.H. Crick, Molecular structure of nucleic acids; a structure for deoxyribose nucleic acid, Nature 171 (4356) (1953) 737–738.
[2] F. Gentile, M. Moretti, T. Limongi, A. Falqui, G. Bertoni, A. Scarpellini, S. Santoriello, L. Maragliano, R.P. Zaccaria, D.F. Enzo, Direct Imaging of DNA Fibers: The Visage of Double Helix, Nano Lett. 12 (12) (2012) 6453–6458.
[3] M. Zhang, K.R. Atkinson, R.H. Baughman, Multifunctional Carbon Nanotube Yarns by Downsizing an Ancient Technology, Science 306 (5700) (2004) 1358–1361.
[4] Y. Gao, F.Y. Guo, P. Cao, J.C. Liu, D.M. Li, J. Wu, N. Wang, Y.W. Su, Y. Zhao, Winding-Locked Carbon Nanotubes/Polymer Nanofibers Helical Yarn for Ultrastretchable Conductor and Strain Sensor, ACS Nano 14 (3) (2020) 3442–3450.
[5] K. Liu, C. Cheng, J. Suh, R. Tang-Kong, D. Fu, S. Lee, J. Zhou, L.O. Chua, J.Q. Wu, Multifunctional Torsional Micromuscles Activated by Phase Transition, Adv. Mater. 26 (11) (2014) 1746–1750.
[6] G. Hwang, H. Hashimoto, D.J. Bell, L.X. Dong, B.J. Nelson, S. Schön, Piezoresistive InGaAs/GaAs Nanosprings with Metal Connectors, Nano Lett. 9 (2) (2009) 554–561.
[7] V.Y. Prinz, V.A. Seleznev, A.K. Gutakovsky, A.V. Chehovskiy, V.V. Preobrazhenskii, M.A. Putyato, T.A. Gavrilova, Free-standing and overgrown InGaAs/GaAs nanotubes, nanohelices and their arrays, Phys. E. 6 (1–4) (2000) 828–831.
[8] O.G. Schmidt, K. Eberl, Thin solid films roll up into nanotubes, Nature 410 (6825) (2001) 168.
[9] A. Cho, Curling Films Turn Themselves Into Nanodevices, Science 313 (5784) (2006) 164–165.
[10] K. Kamata, S. Suzuki, M. Ohtsuka, M. Nakagawa, T. Iyoda, A. Yamada, Fabrication of Left-Handed Metal Microcoil from Spiral Vessel of Vascular Plant, Adv. Mater. 23 (46) (2011) 5509–5513.
[11] A. Elfwing, C. S. Ponseca, L. Q. Ouyang, A. Urbanowicz, A. Krotkus, D. Y. Tu, R. Forchheimer, O. Inganäs, Conducting Helical Structures from Celery Decorated with a Metallic Conjugated Polymer Give Resonances in the Terahertz Range, Adv. Funct. Mater. 28 (24) (2018) 1706595(1−8).
[12] K. Komaba, S. Hirokawa, H. Goto, Preparation of biocarbon micro coils, Soft Mater. 19 (1) (2020) 40–49.
[13] W. Shenton, T. Douglas, M. Young, G. Stubbs, S. Mann, Inorganic-organic nanotube composites from template mineralization of tobacco mosaic virus, Adv. Mater. 11 (3) (1999) 253–256.
[14] L.C. Li, R.Q. Sun, R.L. Zheng, Tunable Morphology and Functionality of Multicomponent Self-assembly: A review, Mater. Des. 197 (2021) 109209.
[15] X.J. Yang, Y.H. Shen, J.Y. Liu, Y.F. Wang, W. Qi, R.X. Su, Z.M. He, Rational Design of Chiral Nanohelices from Self-Assembly of Meso-tetrakis (4-Carboxyphenyl) Porphyrin-Amino Acid Conjugates, Langmuir 37 (44) (2021) 13067–13074.
[16] P.Z. Liu, Y. Battie, M. Decossas, S. Tan, E. Pouget, Y. Okazaki, T. Sagawa, R. Oda, Chirality Induction to CdSe Nanocrystals Self-Organized on Silica Nanohelices: Tuning Chiroptical Properties, ACS Nano 15 (10) (2021) 16411–16421.
[17] L. Ohnoutek, B.J. Olohan, R.R. Jones, X.Z. Zheng, H.H. Jeong, V.K. Valev, Second Harmonic Rayleigh Scattering Optical Activity of Single Ag Nanohelices in a Liquid, Nanoscale 14 (10) (2022) 3888–3898.
[18] Y. Li, Y.Z. Jin, W. Su, L. Pi, K.H. Chen, L. Yan, G. Chen, Nano-TiO_2 anchored carbon nanohelices as reinforcing/anti-aging filler for styrene-butadiene rubber, Mater. Chem. Phys. 285 (1) (2022) 126119.
[19] J. Foroughi, G. M. Spinks, G. G. Wallace, J. Y. Oh, M. E. Kozlov, S. L. Fang, T. Mirfakhrai, Madden, D. W. J. M. K. Shin, S. J. Kim, R. H. Baughman, Torsional Carbon Nanotube Artificial Muscles, Science 334 (6055) (2011) 494−497.
[20] M.D. Lima, N. Li, M.J. Andrade, S.L. Fang, J.Y. Oh, G.M. Spinks, M.E. Kozlov, C.S. Haines, D. Suh, J. Foroughi, S.J. Kim, Y.S. Chen, T. Ware, M.K. Shin, L.D. Machado, A.F. Fonseca, J.D.W. Madden, W.E. Voit, D.S. Galvão, R.H. Baughman, Electrically, Chemically, and Photonically Powered Torsional and Tensile Actuation of Hybrid Carbon Nanotube Yarn Muscles, Science 338 (16) (2012) 928–932.
[21] A.M.K. Esawi, M.M. Farag, Carbon nanotube reinforced composites: Potential and current challenges, Mater. Des. 28 (9) (2007) 2394–2401.
[22] J. Foroughi, G. Spinks, Carbon nanotube and graphene fiber artificial muscles, Nanoscale Adv 1 (12) (2019) 4592–4614.
[23] W.H. Guo, C. Liu, F.Y. Zhao, X.M. Sun, Z.B. Yang, T. Chen, X.L. Chen, L.B. Qiu, X.H. Hu, H.S. Peng, A Novel Electromechanical Actuation Mechanism of a Carbon Nanotube Fiber, Adv. Mater. 24 (39) (2012) 5379–5384.
[24] K.Y. Chun, S.H. Kim, M.K. Shin, C.H. Kwon, J. Park, Y.T. Kim, G.M. Spinks, M.D. Lima, C.S. Haines, R.H. Baughman, S.J. Kim, Hybrid carbon nanotube yarn artificial muscle inspired by spider dragline silk, Nat. Commun. 5 (3322) (2014) 1–9.
[25] E. Smela, Conjugated Polymer Actuators for Biomedical Applications, Adv. Mater. 15 (6) (2003) 481–494.
[26] D.B. Li, R. Baughman, T.J. Huang, J.F. Stoddart, P.S. Weiss, Molecular, Supramolecular, and Macromolecular Motors and Artificial Muscles, MRS Bull. 34 (9) (2009) 671–681.
[27] J. Madde, N.A. Vandesteeg, P.A. Anquetil, P. Madden, A. Takshi, R.Z. Pytel, S.R. Lafontaine, P.A. Wieringa, I.W. Hunter, Artificial muscle technology: physical principles and naval prospects, IEEE J. Oceanic. Eng. 29 (3) (2004) 706–728.
[28] Y. Jang, S.M. Kim, K.J. Kim, H.J. Sim, B.J. Kim, J.W. Park, R.H. Baughman, A. Ruhparwar, S.J. Kim, Self-Powered Coiled Carbon-Nanotube Yarn Sensor for Gastric Electronics, ACS Sens. 4 (11) (2019) 2893–2899.
[29] K.J. Kim, J.S. Hyeon, H. Kim, T.J. Mun, C.S. Haines, N. Li, R.H. Baughman, S.J. Kim, Enhancing the Work Capacity of Electrochemical Artificial Muscles by Coiling Plies of Twist-Released Carbon Nanotube Yarns, ACS Appl. Mater. Interfaces 11 (14) (2019) 13533–13537.
[30] P.N. Chen, S.S. He, Y.F. Xu, X.M. Sun, H.S. Peng, Electromechanical Actuator Ribbons Driven by Electrically Conducting Spring-Like Fibers, Adv. Mater. 27 (34) (2015) 4982–4988.
[31] Y.Y. Shang, X.D. He, C.H. Wang, L.Y. Zhu, Q.Y. Peng, E.Z. Shi, S.T. Wu, Y.B. Yang, W.J. Xu, R.G. Wang, S.Y. Du, A.Y. Cao, Y.B. Li, Large-Deformation, Multifunctional Artificial Muscles Based on Single-Walled Carbon Nanotube Yarns, Adv. Energy Mater. 17 (1) (2015) 14–20.
[32] I.P. Chen, M.C. Yang, C.H. Yang, D.X. Zhong, M.C. Hsu, Y. Chen, Newton Output Blocking Force under Low-Voltage Stimulation for Carbon Nanotube-Electroactive Polymer Composite Artificial Muscles, ACS Appl. Mater. Interfaces 9 (6) (2017) 5550–5555.
[33] S. Aziz, G.M. Spinks, Torsional artificial muscles, Mater. Horiz. 7 (3) (2020) 667–693.
[34] Z.S. Liu, R. Zhang, Y.C. Xiao, J.T. Li, W. Chang, D. Qian, Z.F. Liu, Somatosensitive film soft crawling robots driven by artificial muscle for load carrying and multi-terrain locomotion, Mater. Horiz. 8 (6) (2021) 1783–1794.
[35] X. Zhou, S.L. Fang, X.Q. Leng, Z.F. Liu, R.H. Baughman, The Power of Fiber Twist, Acc. Chem. Res. 54 (11) (2021) 2624–2636.
[36] Y.Y. Li, B.Z. Sun, S. Sockalingam, Z.J. Pan, W.B. Lu, T.W. Chou, Influence of Transverse Compression on Axial Electromechanical Properties of Carbon Nanotube Fibers, Mater. Des. 188 (2020) 108463.
[37] Z.Z. Zhai, L.H. Zhang, T.M. Du, B. Ren, Y.L. Xu, S.S. Wang, J.F. Miao, Z.F. Liu, A Review of Carbon Materials for Supercapacitors, Mater. Des. 221 (2022) 111017.
[38] X.H. Hu, X.F. Bao, J. Wang, X.S. Zhou, H.W. Hu, L.H. Wang, S. Rajput, Z.Q. Zhang, N.Y. Yuan, G.G. Cheng, J.N. Ding, Enhanced Energy Harvester Performance by a Tension Annealed Carbon Nanotube Yarn at Extreme Temperatures, Nanoscale 14 (43) (2022) 16185–16192.
[39] J.T. Di, S.L. Fang, F.A. Moura, D.S. Galvão, J. Bykova, A. Aliev, M.J. Andrade, X. Lepró, N. Li, C. Haines, R.O. Robles, D. Qian, R.H. Baughman, Twist-Stable Carbon Nanotube Yarns and Muscles by Tension Annealing at Extreme Temperatures, Adv. Mater. 28 (31) (2016) 6598–6605.
[40] A.M. Fennimore, T.D. Yuzvinsky, W.Q. Han, M.S. Fuhrer, J. Cumings, A. Zettl, Rotational actuators based on carbon nanotubes, Nature 424 (6947) (2003) 408–410.
[41] F.C. Meng, X.H. Zhang, R. Li, J.N. Zhao, X.H. Xuan, X.H. Wang, J.Y. Zou, Q.W. Li, Electro-Induced Mechanical and Thermal Responses of Carbon Nanotube Fibers, Adv. Mater. 26 (16) (2014) 2480–2485.
[42] P.N. Chen, Y.F. Xu, S.S. He, X.M. Sun, W.H. Guo, Z.T. Zhang, L.B. Qiu, J.F. Li, D.Y. Chen, H.S. Peng, Biologically Inspired, Sophisticated Motions from Helically Assembled, Conducting Fibers, Adv. Mater. 27 (6) (2015) 1042–1047.
[43] J. A. Lee, Y. T. Kim, G. M. Spinks, D. Suh, Lepro, X. M. D. Lima, R. H. Baughman, S. J. Kim, All-Solid-State Carbon Nanotube Torsional and Tensile Artificial Muscles, Nano Lett. 14 (5) (2014) 2664−2669.
[44] A.B. Whitman, C.N. Desilva, An exact solution in a nonlinear theory of rods, J. Elast. 4 (4) (1974) 265–280.
[45] Z. Zhou, P.Y. Lai, B. Jos, Elasticity and stability of a helical filament, Phys. Rev. E. 71 (5) (2005) 052801.
[46] L. Dai, X.J. Huang, L.X. Dong, Q. Zhang, L. Zhang, Mechanically tough, elastic and stable rope-like double nanohelices, Nanoscale 6 (16) (2014) 9436–9442.

[47] J.R. Hutchinson, Shear Coefficients for Timoshenko Beam Theory, J. Appl. Mech. 68 (1) (2001) 87–92.
[48] K.M. Liew, X.Q. He, C.H. Wong, On the study of elastic and plastic properties of multi-walled carbon nanotubes under axial tension using molecular dynamics simulation, Acta Mater. 52 (9) (2004) 2521–2527.
[49] T.K. Truong, Y. Lee, D. Suh, Multifunctional characterization of carbon nanotube sheets, yarns, and their composites, Curr. Appl. Phys. 16 (9) (2016) 1250–1258.
[50] L. Dai, K.D. Zhu, W.Z. Shen, X.J. Huang, L. Zhang, A. Goriely, Controllable rotational inversion in nanostructures with dual chirality, Nanoscale 10 (14) (2018) 6343–6348.
[51] L.L. Xu, Q.Y. Peng, Y. Zhu, X. Zhao, M.L. Yang, S.S. Wang, F.H. Xue, Y. Yuan, Z.S. Lin, F. Xu, X.X. Sun, J.J. Li, W.L. Yin, Y.B. Li, X.D. He, Artificial Muscle with Reversible and Controllable Deformation Based on Stiffness-variable Carbon Nanotube Spring-like Nanocomposite Yarn, Nanoscale 11 (17) (2019) 8124–8132.